Robust Control of Wireless Power Transfer Despite Load and Data Communications Uncertainties

Reza Naghash, Seyed Mohammad Mahdi Alavi, Seyed Ebrahim Afjei

***Abstract*—This paper focuses on the robust control of wireless power transfer (WPT) systems, to work satisfactorily around the desired resonant frequency in the presence of load and data communications uncertainties. The proposed robust control system is based on quantitative feedback theory (QFT), consisting of a feedback compensator and a pre-filter, which are designed by shaping the system's frequency responses, to satisfy the design constraints defined in terms of stability, tracking, and other desired requirements. A feature of QFT is to provide the designer with interactive graphical tools for the design and tuning of the feedback compensator and pre-filter. Without loss of generality, this paper elaborates the design of the QFT-based robust control for a WPT system with a full-bridge inverter and series-series capacitor-based compensation circuits and uncertain direct-current (DC) load. The data communications uncertainties are also addressed in the design. The effectiveness of the proposed QFT-based robust control methodology is evaluated through simulations, practical experiments, and compared with H_∞ and Skogestad internal model control (SIMC) design methods. Due to the fact that QFT is a model-based approach, this paper also elaborates small-signal transfer function modeling of WPT systems.**

***Index Terms*—Wireless Power Transfer, Inductive Power Transfer, Robust Control, Uncertain Systems, Quantitative Feedback Theory (QFT), Data Communications Uncertainties.**

I. Introduction

Because of easy adaptation, galvanic isolation, portability, and high reliability in harsh environments, wireless or inductive power transfer (WPT or IPT) system is gaining popularity, and has been a promising technology for various applications in transportation electrification [1]–[3], electric appliances [4], robotics [5], and biomedical engineering [6].

This paper focuses on robust voltage control of WPT systems with direct-current (DC) loads such as batteries. A general structure of the whole system is shown in Figure 1. The WPT system aims to transfer the power from one side to another by using two coupled magnetic coils. The responsibility of the robust voltage control system is to regulate the output voltage, V_o, at the desired value in the presence of uncertainties. The output voltage V_o is transmitted to the control system by using wireless communications. A typical DC-load WPT system consists of three main parts as shown in Figure 1: inverter, impedance network, and rectifier. By using an inverter, the input DC is converted to an alternative current (AC), which passes through the transmitter or primary coil, L_P, to create a high frequency oscillating magnetic field. The oscillating magnetic field passes through the receiving or secondary coil, L_S, which induces an alternating electromotive force (EMF) voltage, which in turn creates an AC that is rectified to drive the DC load.

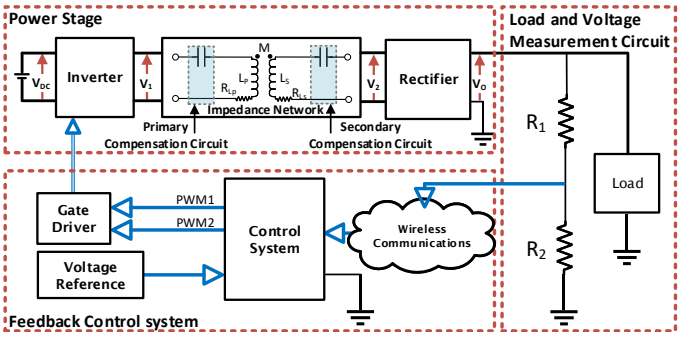

Fig. 1. General structure of wireless power transfer (WPT) systems with voltage-mode control.

Due to high reluctance of the air, mutual inductance significantly diminishes in WPT systems [7], [8]. In addition, distance and misalignment of the primary and secondary coils deteriorate the performance of the power transfer [9]. In order to address these issues and improve the system efficiency in terms of power and quality factors and control purposes, two compensation circuits are added to the primary and secondary sides, [10]–[14]. The compensation circuits are designed such that the WPT system works in a resonant mode, where the reactance, i.e., imaginary part, of the impedance network is zero, and maximum power transfer is achieved. The desired resonant frequency depends on the application, thus the selection of the compensation circuits varies from one application to another. In Figure 1, *series-series* (*SS*) compensation circuits are used, where two capacitors are connected in series with the primary and secondary coils. Other well-known capacitor-based compensation circuits include: *series-parallel* (*SP*), *parallel-series* (*PS*), and *parallel-parallel* (*PP*), [15]. Compensation circuits with a network of inductors and capacitors are also used in some designs, [1], [16]–[20].

Control plays a key role in WPT systems. Various control methodologies have been developed, based on phase shift [1], [17]–[19] or pulse-width-modulation (PWM) [12], [16], [21]–[28], for the regulation of output voltage [12], [17], [21], [25], output current [16], [18], output power [1], [19], [22], [23], [27], input current [16], [24] at fixed [1], [12], [16]–[19], [21]–

R. Naghash is with the Faculty of Electrical Engineering, Shahid Beheshti University, Velenjak, Tehran, Iran. E-mail: re.naghash@gmail.com

S. M. M. Alavi is with the Department of Electrical and Computer Engineering, University of Windsor, Windsor, ON, Canada. E-mail: mahdi.alavi.work@gmail.com, mahdi.alavi@uwindsor.ca (*Corresponding Author)*

S. E. Afjei is with the Faculty of Electrical Engineering, Shahid Beheshti University, Velenjak, Tehran, Iran. E-mail: e-afjei@sbu.ac.ir

[26], [28] or variable [27], [29], [30] resonant frequencies. As the control of DC-DC converters is well-established, in some works, front-side and/or back-side DC-DC converters are added to the WPT circuit, to simplify the control system design [12], [23], [24]. However, additional high frequency DC-DC converter might increase the electromagnetic interference, and the production and maintenance cost. In the majority of these papers, the well-known proportional-integral (PI) controller is used [1], [5], [16]–[19], [21], [22], [25], [27], [28]. In [19], a Ziegler-Nichols based method is proposed for tuning the parameters of the PI controller. However, there is still a significant lack of information and standard methodology for tuning the PI parameters in WPT systems applications. Uncertainty due to the variation of magnetic and load parameters, as well as the misalignment of primary and secondary coils are also of important issues, which cause power fluctuations and degrade the system performance. In [1], [21], [22], [28], different techniques are proposed for the robustness evaluation of WPT control systems based on experimental, sensitivity, and stability analysis methods. In [15] and [31], the design of standard and two-degree-of-freedom $H_\infty-$based robust control systems is discussed for SS-WPT systems, where the SS compensation circuits are used. In [32], a method is developed for optimal H_∞ control of SS-WPT systems by using genetic algorithms. Overall, there is still a significant demand for systematic design techniques for robust control of WPT systems despite uncertainties.

This paper focuses on the model-based control, where a transfer function or state-space model of the WPT system is required. In [15], generalized state-space averaged (GSSA) modeling of the SS-WPT system is developed. In [18] and [19], state-space modeling of unidirectional and bidirectional WPT system with LCL impedance networks is addressed. By using the coupled mode theory, an averaged state-space model of a half bridge SS-WPT is derived in [12]. Modeling of the SS-WPT system with front-side and load-side DC-DC converters is discussed in [21] by using the generalized averaging technique [33]. In [16], a sequential approach is applied to obtain a transfer function of the WPT system with LCL and S compensations circuits at the primary and secondary sides. In this approach, the transfer functions of all components are obtained individually, and coupled together at the end.

In this paper, quantitative feedback theory (QFT) is developed for robust control of WPT systems to work satisfactorily around the desired resonant frequency in the presence of existing uncertainties. The QFT-based robust control system consists of a feedback compensator and a pre-filter. The feedback compensator is designed to achieve a satisfactory level of robustness despite uncertainties. The pre-filter is designed so as to shift the closed-loop system's response to the desired tracking region. In the proposed robust control technique, design objectives are formulated as inequality constraints on the system transfer functions, which result in graphical bounds in the Nichols chart and Bode diagram. The feedback compensator and pre-filter are designed such that these graphical design bounds are satisfied. The graphical design bounds provide interactive tools for the selection and tuning of the feedback compensator and pre-filter. The proposed robust control technique is also capable of handling all uncertainties on the load parameters, magnetic coupling coefficient or mutual inductance variations. Without loss of generality, this paper elaborates the design of the QFT-based robust control system for a WPT system with a full-bridge inverter, and series-series capacitor-based compensation circuits. The voltage of the WPT system is robustly controlled under direct-current (DC) uncertain loads. This paper also considers the data communications uncertainties, which are given in terms of packet drop and data transmission time-delay. Both simulation and experimental results are presented and compared with the fixed-structured H_∞ [34] and Skogestad internal model control (SMIC) [35], [36] tuning approaches.

A. Contributions of This Paper

- This paper elaborates a general method for small-signal transfer function modeling of WPT systems.
- This paper proposes a robust control system, which considers uncertainties of the load and data communications together.
- To the best of our knowledge, this is the first paper, elaborating the design of QFT-based robust control over WPT systems with practical tests. In the past, QFT has been developed and applied to a wide range of applications in wind energy systems [37], DC-DC converter control [38], impedance spectroscopy [39], chemical processes [40], wireless sensor networks [41], robotics [42], [43].

B. Outlines

The rest of the paper is organized as follows. Experimental setup, its topology, and transfer function modeling are described in Section II. The design of the QFT-based robust control system is elaborated in Section III. The effectiveness of the proposed design methodology is evaluated through simulations, practical experiments, and comparative studies in Section IV.

II. Experimental Setup, Topology and Modeling

This paper focuses on the SS-WPT system Figure 2, which has widely been addressed in the literature [12], [15], [22]–[25], [28]–[30], [32], with a full-bridge inverter and rectifier, and SS compensation circuits. Further information about the

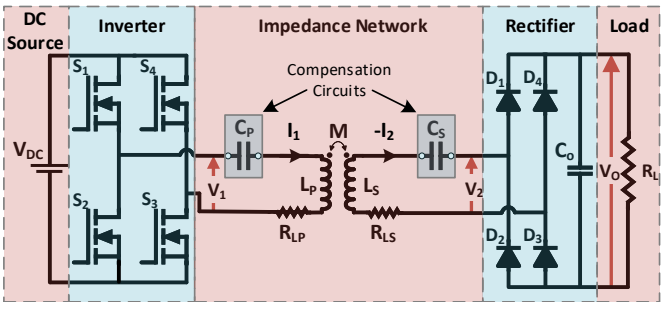

Fig. 2. A typical structure of wireless power transfer (WPT) system, with series-series (SS) compensation circuits.

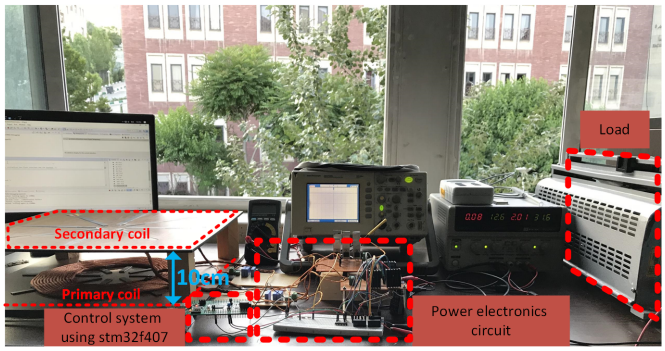

Fig. 3. A photo of the experimental setup.

SS compensation circuits, and computation of C_S and C_P are provided in Section S.I. of the supplementary material. In this section, the data of the experimental setup are provided, which are used throughout this paper. Then, transfer function models of the full-bridge SS-WPT system and wireless data communications are developed.

A. Experimental Setup

Figure 3 shows a photo of the experimental set-up, designed based on the technical information and hints in [2] and references therein. Two circular coils are fabricated with the external radius of $15.5cm$ and internal radius of $8.5cm$, made from a Litz wire. The Litz wire is made out of 840 thinner insulated $0.1mm$ wires. The number of wire turns for both coils is 13. By using an RLC meter, the inductance and internal resistance of the coils are measured as follows: $L_P = 79.8\mu H$, $L_S = 79\mu H$, $R_{L_p} \approx R_{L_s} \approx 0.08\Omega$. The measured mutual inductance is $M = 26.9\mu H$, which is equivalent to around 33% coupling factor. 64 ferrite bars, 32 at the primary side and 32 at the secondary side, are utilized to decrease the reluctance path between the primary and secondary coils. The length of each ferrite bar is $4cm$. The output capacitor is chosen $C_o = 220\mu F$. After some computations, which are discussed later in this section, the capacitors of the SS compensation circuits are chosen as $C_P = 45.1nF$, and $C_S = 45.7nF$, which result in a resonant frequency of

$$f_r = 83.7kHz, \tag{1}$$

which is adequately close to the resonant frequency $85kHz$ in electric vehicles applications as per SAE J2954 standards [46]. Discussion about the selection of the desired resonant frequency is beyond the scope of this paper. Several parameters such as switching losses and quality factor need to be considered. Interested readers are directed to [47] and references therein for a more comprehensive information on this subject.

It should also be noted that fundamentals of modeling, analysis, and design of robust control system do not change with these numerical data and components values.

B. Small-Signal Transfer Function Modeling of the Power Stage and Load

In the voltage-mode control of WPT systems, the objective is to keep the output voltage stable and as close as possible to the desired value despite uncertainties. As shown in Figure 1, the output voltage, V_o, is measured and is transmitted to the control system by using wireless communications. The received data of the output voltage is compared with the desired value, and the error is then fed into the control system to generate the desired control signal. Since, the duty cycle of the PWM signals affects the peak of the fundamental harmonic of the output voltage in the resonant converters [48], this work focuses on the duty-cycle based control signal. A single duty cycle, d, is enough for the control of the full-bridge inverter Figure 2, because the PWM signals applied to the gates of S_1 and S_3 are identical and toggled of the identical PWM signals, applied to the gates of S_2 and S_4.

In this section, an overall small-signal transfer function of the power stage and load, G_{sys}, is derived as follows:

$$G_{sys}(s) = \frac{\tilde{v}_o(s)}{\tilde{d}(s)}. \tag{2}$$

where, s is the Laplace operator, and $\tilde{v}_o(s)$ and $\tilde{d}(s)$ are the small signals of the output voltage and duty cycle, respectively. The 'tilde' symbol represents 'small signal'. The transfer function $G_{sys}(s)$ is split into three parts as follows:

$$G_{sys}(s) = G_{inv}(s)G_{net}(s)G_{rec}(s), \tag{3}$$

where, $G_{inv}(s)$, $G_{net}(s)$, and $G_{rec}(s)$ denote the transfer functions of the inverter, impednace network, and rectifier, respectively, given by:

$$G_{inv}(s) = \frac{\tilde{v}_1(s)}{\tilde{d}(s)},\ G_{net}(s) = \frac{\tilde{v}_2(s)}{\tilde{v}_1(s)},\ G_{rec}(s) = \frac{\tilde{v}_o(s)}{\tilde{v}_2(s)}. \tag{4}$$

In the following, these transfer functions are computed.

1) Small-signal transfer function of the inverter: Figure 4 shows the inverter's gates and output voltage signals in one cycle of its normal operation. The gate signal $V_{gs\ S1,S3}$ is applied to switches S_1 and S_3, and is toggled of the gate signal $V_{gs\ S2,S4}$ that is applied to switches S_2 and S_4. Each of the gate signals is high for DT_s seconds, where D is the steady-state duty cycle, T_s is the switching time period. The Fourier series expansion of the output square-wave voltage results in:

$$v_1(t) = \frac{4V_{DC}}{\pi}\sum_{n=1}^{\infty}\frac{1}{(2n-1)}\sin(2(2n-1)\pi f_s t) \tag{5}$$

where, $f_s = 1/T_s$ represents the switching frequency. Since the inverter is operated at the resonant frequency, its voltage and current signals are in phase, and the phase shift between the legs is equal to $\pi(rad)$. At the resonant frequency, the impedance network basically responds to the fundamental harmonic and not to higher harmonic frequencies. Thus, the inverter output voltage is approximated by its fundamental component as follows:

$$v_1(t) \approx v_1^{fundamental}(t) = \frac{4V_{DC}}{\pi}\sin(2\pi f_s t) \tag{6}$$

When the switching frequency is close enough to the resonant frequency, this approximation is more evident. By considering the duty cycle d, the output voltage v_1 is given by,

$$v_1(t) = \frac{4V_{DC}}{\pi}\sin(\omega_s t)\sin(\pi d) \tag{7}$$

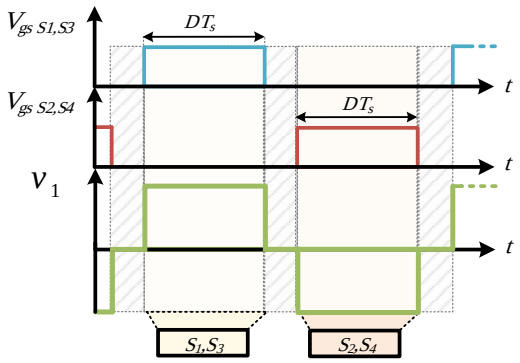

Fig. 4. Inverter's gates and output voltage signals in one cycle of its normal operation.

Figure 5 shows the sinusoidal approximation of the inverter's output voltage for $d = 50\%$ and $d = 40\%$. It is seen that the peak of the fundamental harmonic of the output voltage depends on the duty cycle. Thus, the peak of v_1, i.e., v_1^{peak} is used for the voltage control as follows:

$$v_1(t) \simeq v_1^{peak}(t) = \frac{4V_{DC}}{\pi}\sin(\pi d) \tag{8}$$

It should be noted that the phase of the fundamental harmonic varies with the duty cycle. However, for the resistive load in this paper, the voltage and current signals remain in phase.

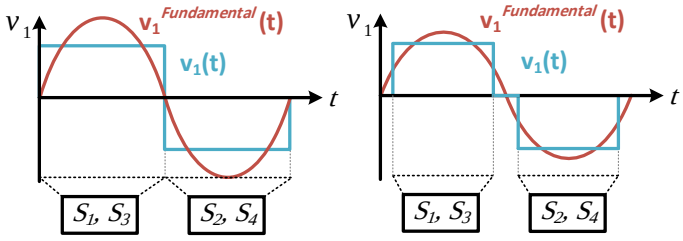

(a) d=50% (b) d=40%

Fig. 5. Fundamental harmonic of the inverter's output voltage for $d = 50\%$ and $d = 40\%$.

By defining the following small perturbations on the duty cycle and output voltage signals,

$$v_1 = V_1 + \tilde{v}_1$$
$$d = D + \tilde{d},$$

equation (7) is re-written as follows:

$$V_1 + \tilde{v}_1(t) = \frac{4V_{DC}}{\pi}\sin(\pi D + \pi\tilde{d})$$
$$= \frac{4V_{DC}}{\pi}\Big(\sin(\pi D)\cos(\pi\tilde{d}) + \cos(\pi D)\sin(\pi\tilde{d})\Big)$$

By using the approximations of $\sin(\pi\tilde{d}) \simeq \pi\tilde{d}$ and $\cos(\pi\tilde{d}) \simeq 1$ for small $\tilde{d}$, a small-signal representation of (7) is obtained as follows:

$$\tilde{v}_1 = 4V_{DC}\tilde{d}\cos(\pi D). \tag{9}$$

Subsequently, the small-signal transfer function $G_{inv}(s)$ is obtained as follows:

$$G_{inv}(s) = 4V_{DC}\cos(\pi D) \tag{10}$$

2) Small-signal transfer function of the impedance network: For the derivation of the small-signal transfer function of the impedance network, the equivalent circuit Figure S1 (from the supplementary material) is applied. It is clear that:

$$G_{net}(s) = \frac{\tilde{v}_2(s)}{\tilde{v}_1(s)} = \frac{\tilde{v}_2(s)}{\tilde{v}_M(s)}\frac{\tilde{v}_M(s)}{\tilde{v}_1(s)} \tag{11}$$

By defining the following parameters,

$$Z_P = R_{L_P} + s(L_P - M) + \frac{1}{sC_P},$$
$$Z_S = R_{L_S} + s(L_S - M) + \frac{1}{sC_S},$$
$$Z_M = sM,\ R_{L,ac} = \frac{8}{\pi^2}R_L,$$

and using the Kirchhoff's voltage and current laws, these transfer functions are obtained as follows:

$$\frac{\tilde{v}_M(s)}{\tilde{v}_1(s)} = \frac{R_{L,ac}Z_M + Z_SZ_M}{R_{L,ac}Z_M + Z_SZ_M + R_{L,ac}Z_P + Z_SZ_P + Z_MZ_P} \tag{12}$$

$$\frac{\tilde{v}_2(s)}{\tilde{v}_M(s)} = \frac{R_{L,ac}}{R_{L,ac} + Z_S} \tag{13}$$

The transfer function G_{net} is then obtained by the multiplication of (12) and (13) as follows:

$$G_{net}(s) = \frac{R_{L,ac}Z_M}{R_{L,ac}Z_M + Z_SZ_M + R_{L,ac}Z_P + Z_SZ_P + Z_MZ_P} \tag{14}$$

Figure 6 shows the bode plot of G_{net}, for various loads. It is highlighted that the gain significantly varies around the resonant frequency $f_r = 83.7kHz$ with respect to the load, which emphasizes the need for robust control.

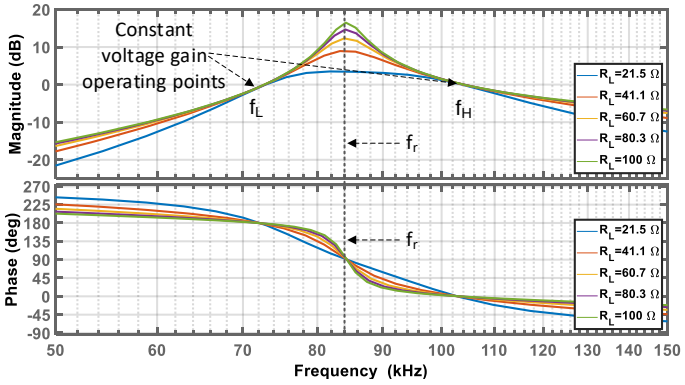

Fig. 6. Bode plot of the impedance network G_{net} under the load variations.

3) Small-signal transfer function of the rectifier: The Kirchhoff's current law at the output node results in:

$$C_o\frac{dv_o}{dt} =< i_2 > -i_o \tag{15}$$

where, i_o is the load's current. Since the average of i_2 is zero over a switching cycle is zero, its half-cycle average, i.e., $< i_2 >$, is considered. By ignoring the diodes' internal resistances, $< i_2 >= v_2/R_L$. The output voltage v_o is also equal to i_oR_L, thus,

$$C_o\frac{dv_o}{dt} = \frac{v_2}{R_L} - \frac{v_o}{R_L}. \tag{16}$$

The small-signal transfer function of the rectifier is obtained by taking the Laplace transform of (16) as follows:

$$G_{rec} = \frac{\tilde{v}_o(s)}{\tilde{v}_2(s)} = \frac{1}{R_LC_os+1} \tag{17}$$

The accuracy of the derived small-signal transfer functions is verified in Section S.II. of the supplementary material.

C. Modeling of the Wireless Communication

Wireless communication is mainly modeled based on transmission time-delays and packet dropouts. Time-delay refers to the time that is required for the transmission of the output voltage data to the control system. Packet dropout occurs when the data of the output voltage is not received at the control system, due to wireless channel conditions, high bit-error-rate of the received data, significant transmission time-delay, etc. Similar to many networked control systems [49], [50], the transmission time-delays and packet dropouts are modeled as an uncertain time-delay transfer function as follows:

$$G_{delay} = e^{-t_ds} \tag{18}$$

where t_d is time-varying and a multiple of the sampling frequency, i.e., $t_d = kT_{sampling},\ k = 0, 1, 2, \cdots, k_{\max}$; $k = 0$ implies the perfect wireless communication with no packet drop and transmission time-delay; $k_{\max}$ denotes the maximum allowable data transmission time-delay.

III. Control System Design

It is observed from Figure 6 that the impedance network with the SS compensation circuits operates as a constant gain under the load variations at f_L and f_H. In some works, it is suggested to control the operation of the WPT system at one of these two frequencies, [11]. However, the system does not work in the full resonant mode at f_L or f_H, i.e, the total inductance is not fully compensated, and the impedance is not fully resistive at these frequencies. Thus, it can be shown that the total power transfer decreases by 28% and 80% at f_L or f_H. In contrast, it is shown that robust control of the WPT systems at the resonant frequency f_r significantly improves the overall power transfer. However, operation of the WPT system at f_r might decrease the efficiency, compared to the operation at f_L or f_H. It was mentioned in the literature that this drawback of the operation at f_r will significantly be resolved by the future technology of the switching semiconductors [25]. Section S.III. in the supplementary material provides further results and discussions about operations at f_r, and the conditions required for having zero-voltage-switching (ZVS).

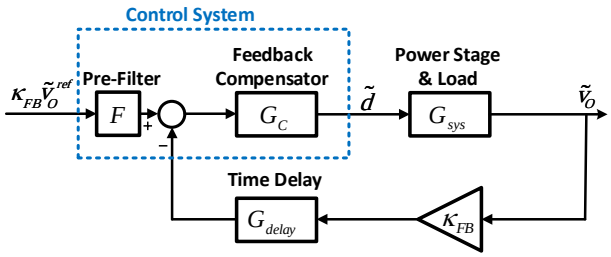

Fig. 7. Block diagram of the WPT system with QFT-based control.

Based on these statements, this paper focuses on the control of WPT system at the resonance frequency f_r to transfer the maximum power. However, the variations of the magnitude responses for various loads at f_r, as shown in Figure 6, emphasize the need for a robust control system. Thus, a QFT-based robust control system is designed in this paper for the given SS-WPT circuit at the resonant frequency f_r under the load variations.

The control system is composed of a pre-filter, $F(s)$, and a feedback compensator, $G_C(s)$, as shown in Figure 7. The feedback compensator guarantees stability, and reduces the effects of uncertainties on the system performance. The pre-filter shifts the closed-loop system response to the desired tracking region. At the first stage of the design, the desired specifications such as stability and tracking performance are formulated as inequality constraints on the system's transfer functions. The solution of the inequality constraints results in some graphical designs in the Nichols chart for the design of $G_C(s)$, and in the bode plot for the design of $F(s)$. In the second stage of the design, the feedback compensator and pre-filter are designed by shaping the system's frequency response such that the graphical designs are satisfied. Interested readers are directed to [44] for the theoretical aspects of QFT.

A. Design Constraints

Two design constraints are defined, one for tracking and one for robust stability.

For tracking performance, the following constraint is applied

$$|D_l(j\omega)| \le \left|F\frac{G_CG_{sys}}{1+L_f}(j\omega)\right| \le |D_u(j\omega)|\,,\ \text{for } \omega \in \{\omega_t\} \tag{19}$$

which, puts the closed-loop system between an upper bound D_u, and a lower bound D_l over the uncertainty region. In the design, it is sufficient to compute and satisfy the tracking constraint (19) for a set of frequencies, $\{\omega_t\}$, within the bandwidth. The upper and lower bounds D_u and D_l are chosen with respect to the desired overshoot, settling time, bandwidth, etc. In this example, it is assumed that an overshoot around 5%, and a settling time around $t = 0.1$(s), i.e., a closed-loop

bandwidth around $100rad/sec$ are desired. Thus, the following D_u and D_l are chosen:

$$D_u(s) = \frac{\frac{s}{200}+1}{\frac{s^2}{120^2}+\frac{1.4s}{120}+1} \tag{20}$$

$$D_l(s) = \frac{1}{\left(\frac{s^2}{60^2}+\frac{2s}{60}+1\right)\left(\frac{s}{80}+1\right)} \tag{21}$$

The tracking frequencies are chosen within the closed-loop bandwidth as $\omega_t = 2\pi \times \{0.001, 0.01, 0.1, 1, 10, 100\}(rad/sec)$.

For the robust stability, the following constraint is solved, mainly for the frequencies around and above the bandwidth, where the loop function approaches the critical point (-180°,0dB).

$$\left|\frac{L_f}{1+L_f}(j\omega)\right| \leq \gamma \text{ for } \omega \in \{\omega_s\} \tag{22}$$

where, L_f is the loop-function given by

$$L_f(s) = G_C(s)G_{sys}(s)G_{delay}(s) \tag{23}$$

The satisfaction of (22) guarantees the following gain and phase margins over the uncertainty region [44],

$$\text{Gain Margin} = 1 + \frac{1}{\gamma} \tag{24}$$

$$\text{Phase Margin} = 180° - \frac{360°}{\pi}\cos^{-1}\left(\frac{0.5}{\gamma}\right) \tag{25}$$

In this work, $\gamma = 1.2$ is chosen, which implies the gain and phase margins of 1.83, and 49.2°, respectively. In the literature, anything greater than 45° is usually acceptable, [40], [44], [51]. The stability constraint (22) is solved for $\omega_s = 2\pi \times \{100, 500, 1000\}$.

More constraints for disturbance rejection, noise attenuation, etc., could simply be added using the same approach.

B. Design of Feedback Compensator $G_C(s)$

The constraints (22) and (19) are solved separately in the polar coordinates, for each of the design frequencies $\{\omega_s\}$ and $\{\omega_t\}$. References [44] and [40] explain the computations of the QFT bounds. The QFT Matlab toolbox [45] is used the design. Because of the computations in the polar coordinates, QFT is able to handle the time delay without any Pade approximation. The solutions divide the Nichols chart into acceptable and unacceptable regions at each frequency. The intersection of the accepted regions is chosen for the design of G_C. The design bounds are computed for the maximum time-delay, $k_{\max} = 5$. The QFT control system is implemented on the STM32F407 microcontroller with the clock of analog-to-digital (ADC) conversion equals to $21MHz$, with 12 bits resolution. Fifteen cycles is required for each ADC, thus, the sampling frequency is approximately $T_{sampling} = 15/(21 \times 10^6) = 0.71\mu sec$. Figure 8 shows the intersection of the design bounds obtained from the constraints (19) and (22) in the Nichols chart. The feedback compensator $G_C(s)$ is designed such that the loop function L_f is located inside the overall accepted region, above the solid lines and below the dashed lines, for all design frequencies $\{\omega_s\}$ and $\{\omega_t\}$. At high frequencies, the design bounds are contours, which guarantee the achievement of the desired phase and gain margins.

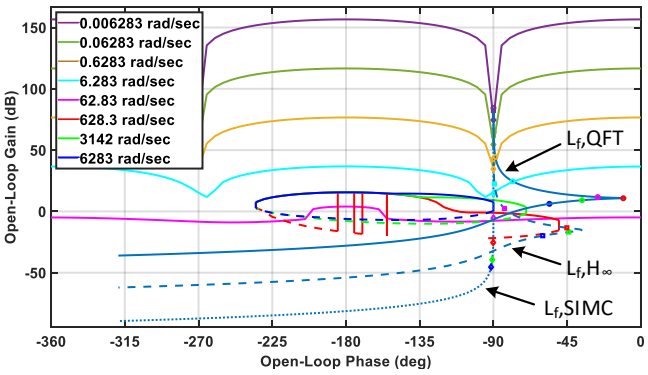

Fig. 8. Nichols chart, which is used for the design of the feedback compensator. This figure shows the QFT design bounds and the loop functions achieved by the QFT (26), SIMC (29), and H_∞ (30) PI controllers. The loop-function with the H_∞ PI controller (30) also satisfies the QFT bounds. The QFT loop-shaping could result in many possible feedback compensators. The loop-function with the SIMC controller (29) does not satisfy some QFT bounds.

The QFT graphical design environment provides the designer with an interactive tool for the design of various lead-lag, PI, or other more complex controllers, by shaping the system frequency response. Because of the popularity of PI controllers, this paper focuses on the design of the PI controller. Figure 8 shows that by using the following PI controller,

$$G_C(s) = 1.267\left(1 + \frac{1}{0.0333s}\right), \tag{26}$$

the loop-function $L_f(s)$ satisfies the design bounds at each design frequency.

C. Design of Pre-filter $F(s)$

In QFT, the pre-filter is designed such that the frequency response of $|FG_CG_{sys}/(1+L_f)|$ is located between the upper and lower bounds $|D_u|$ and $|D_l|$ in the bode magnitude's plot. As shown in Figure 9-b, this condition is satisfied by using the following pre-filter for the given SS-WPT system,

$$F(s) = \frac{1}{(\frac{1}{180}s+1)(\frac{1}{178}s+1)}. \tag{27}$$

Remark 1: In some QFT designs, Smith predictor block is added into the QFT system structure for the time-delay compensation, [51], [52]. The results in this paper show that the WPT system is able to meet the desired specifications without Smith predictor.

IV. Simulation and Experiential Results

A. The Results of the QFT Control System

For the test, the input power supply is set to $V_{DC} = 31.5V$. The distance between the primary and secondary coils is fixed at $10cm$. The desired output voltage is defined at $V_o = 36V$. Simulation and practical tests are run for several loads equals to and higher than $R_L = 22\Omega$. The value of $R_L = 22\Omega$ for the test is obtained by solving (14) at the resonant frequency, for

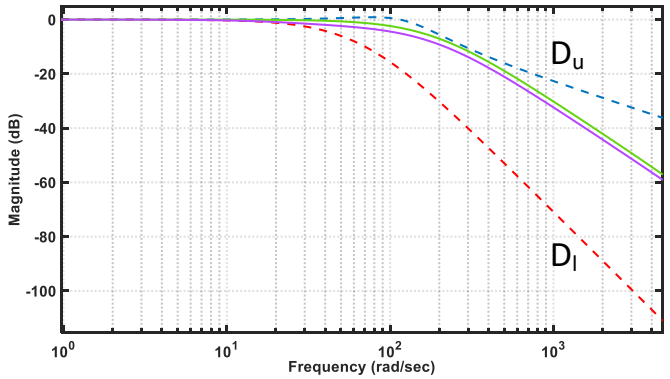

Fig. 9. Bode's magnitude diagram, which is used for the design of the pre-filter to locate the input-output frequency response, from the reference input $r(t)$ to the output $y(t)$ between D_l and D_u. The solid lines show the upper and lower responses of the controlled system.

$v_1 = 31.5$, and $v_2 = 36V + v_{loss,rec}$, where $v_{loss,rec}$ denotes the voltage loss of the diodes. Figure S4 in the supplementary material shows the simulation results of the time-domain step response of the open-loop (uncontrolled) and controlled SS-WPT system, when the load changes from $R_L = 22$ to 100Ω under the perfect wireless communications, i.e., $k = 0$ in (18). It is seen that the open-loop system response is outside the desired region, while the QFT-based control shifts all responses between D_l and D_u.

Figure 10 shows the experimental results. Figure 10-a shows the results for three different loads under perfect wireless communications, i.e., $k = 0$ in (18). Figure 10-b compares the results under time-delay conditions. Similar to [53], time-delays are simulated in the STM32407 microcontroller, which means that the data is collected through ADC in real-time, and transferred to the control system according to the delay. For instance, in the case of one-step delay, the data of the previous sample time is transferred to the control system at each time. For all cases, similar to the simulation results, the outputs of the WPT system are robustly located between D_u and D_l with overshoots of less than 5% and settling times of less than $t = 0.1s$.

Figure S5 in the supplementary material shows the gates' signals S_1 to S_4. It shows that the PWM's duty cycle appropriately changes with respect to the load variations, in order to satisfy the robust control requirements. The signals of the inverters, coils, and rectifies are shown in Figure S6 in the supplementary material, which match the theoretical principles.

The output power, P_o, and efficiency, η, are calculated versus load variations by using

$$\eta = \frac{P_o}{P_{in}} = \frac{V_o^2/R_L}{V_{in}I_{in}} \tag{28}$$

Figure 11 shows the results that they almost linearly decrease with the increase of R_L. The output power is around 62W for $R_L = 22\Omega$, and decreases to around 26W for $R_L = 50\Omega$. The efficiency is around 88% for $R_L = 22\Omega$, and decreases to around 66% for $R_L = 50\Omega$. These results are also similar to the literature [54].

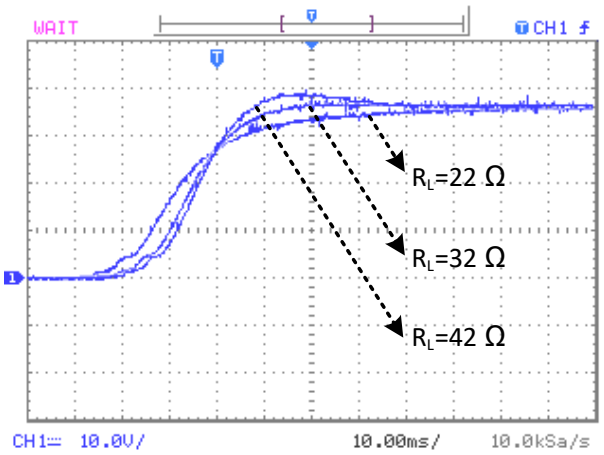

(a) To load variations.

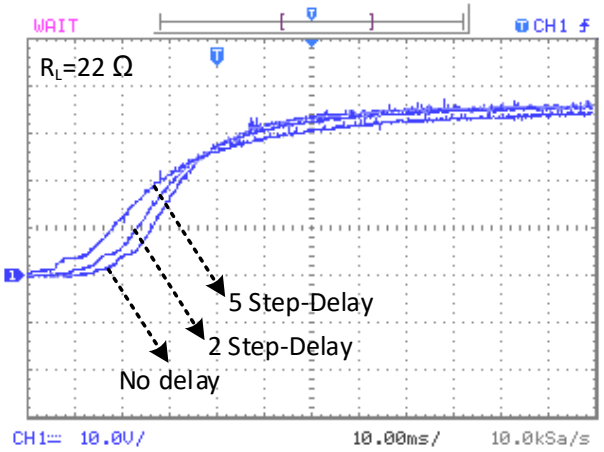

(b) To the delay of data communications.

Fig. 10. Experimental results of the designed QFT robust control system.

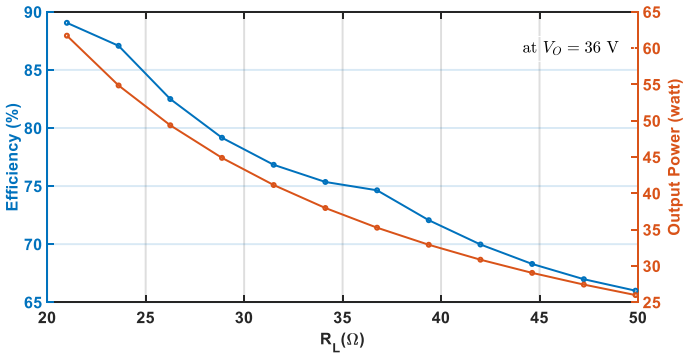

Fig. 11. Experiments: Efficiency and output power of the proposed WPT system versus various loads.

Section S.III. in the supplementary material provides further results and discussions about operation at f_r, and the conditions required for having zero-voltage-switching (ZVS).

B. Comparison

The effectiveness of the QFT-based control is compared with the following PI controllers:

$$G_{C,\text{SIMC}}(s) = 0.0027\Big(1 + \frac{1}{2.2 \times 10^{-4} s}\Big), \tag{29}$$

$$G_{C,H_\infty}(s) = 0.0632\Big(1 + \frac{1}{0.002 s}\Big), \tag{30}$$

achieved through the fixed-structure H_∞ [34] and Skogestad internal model control (SIMC) [35], [36] methods, respectively. In this comparative study, it was tried to use the same weighting functions for both the QFT and H_∞ methods, for the sake of consistency. The design of the H_∞ and SIMC PI controllers is explained in Section S.IV. of the supplementary material.

Figure 8 shows that the loop-function achieved by the H_∞-based PI controller (30) meets also the QFT design bounds. As mentioned earlier, many possible feedback compensators could be achieved satisfying the design bounds. It is also seen from Figure 8 that the loop-function with the SIMC controller (29) does not meet some of the QFT design bounds.

Figure 12 shows the experimental results for the designed QFT, SIMC, and H_∞ controllers for $R_L = 22\Omega$. It is seen that all controllers result in stable input-output system response. The QFT, and H_∞ controllers result in close responses, located between D_l and D_u with satisfactory settling time and overshoot. The DC gain of the SIMC controller is the smallest, leading to slowest system response among the designed controllers.

It should be noted that the proposed QFT, H_∞ and SIMC designs are adjustable by weighting functions in QFT and H_∞ method, and by the nominal plant chosen for the parameter tuning in the SIMC method.

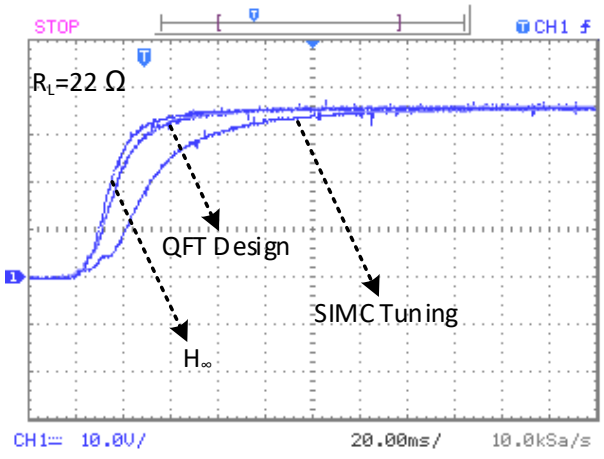

Fig. 12. Experiments: Comparison between the designed QFT, SIMC, and H_∞ controllers for $R_L = 22\Omega$.

V. Conclusions and Future Works

This paper has investigated transfer function modeling of wireless power transfer (WPT) systems, and their systematic robust control by shaping the system's frequency responses through quantitative feedback theory (QFT). The proposed modeling technique is applicable to other WPT systems topologies. QFT quantitatively controls the robust stability and performance of the WPT system at the resonant frequency in the presence of uncertainties. The control signal is the PWM of the inverter switches. The uncertainties of the load and wireless communications have been addressed in this work. The proposed robust control methodology provides a graphical tool for tuning of the controllers for WPT systems. This paper also demonstrated that there is no need to add DC-DC converters to WPT systems for their model-based (robust) control. The proposed QFT-based robust control technique was applied to a WPT system with a full-bridge inverter, capacitor-based compensation circuits, and uncertain direct-current (DC) load, changing between 22 and 100Ω. Promising results were achieved through extensive simulations and experiments. The output voltage response was regulated with overshoots less than 5% and settling times less than $0.1s$ despite load variations, according to the pre-defined upper and lower tracking limits. The proposed QFT-based robust control was extensively compared with H_∞, and SIMC based PI controllers. The selection of the nominal plant for optimal SIMC-based PI control, optimal QFT design [55], [56], and development of the proposed QFT-based controlled WPT system to battery chargers applications are few topics suggested for future research.

References

[1] Y. Tang, Y. Chen, U. K. Madawala, D. J. Thrimawithana, H. Ma, "A New Controller for Bidirectional Wireless Power Transfer Systems," *IEEE Trans. on Power Electronics*, vol. 33, no. 10, pp. 9076 – 9087, Oct. 2018.

[2] R. Tavakoli, Z. Pantic, "Analysis, Design, and Demonstration of a 25-kW Dynamic Wireless Charging System for Roadway Electric Vehicles," *IEEE Journal of Emerging and Selected Topics in Power Electronics*, vol. 6, no. 3, pp. 1378 – 1393, Sept. 2018.

[3] G. A. Covic, J. T. Boys, "Inductive Power Transfer," *Proceedings of the IEEE*, vol. 101, no. 6, pp. 1276 – 1289, June 2013.

[4] Q. Li, Y. C. Liang, "An Inductive Power Transfer System With a High-Q Resonant Tank for Mobile Device Charging," *IEEE Trans. on Power Electronics*, vol. 30, no. 11, pp. 6203 – 6212, Nov. 2015.

[5] C. T. Rim, C. Mi, "Two-Dimensional Omnidirectional IPT for Robots," *Wireless Power Transfer for Electric Vehicles and Mobile Devices*, Wiley-IEEE Press, pp. 563 – 576, 2017.

[6] S. C. Tang, T. L. T. Lun, Z. Guo, K. Kwok, N. J. McDannold, "Intermediate Range Wireless Power Transfer With Segmented Coil Transmitters for Implantable Heart Pumps," *IEEE Trans. on Power Electronics*, vol. 32, no. 5, pp. 3844 – 3857, May 2017.

[7] J. T. Boys, G. A. J. Elliott, G. A. Covic, "An Appropriate Magnetic Coupling Co-Efficient for the Design and Comparison of ICPT Pickups," *IEEE Trans. on Power Electronics*, vol. 22, no. 1, pp. 333 – 335, Jan. 2007.

[8] E. R. Joy, A. Dalal, P. Kumar, "Accurate Computation of Mutual Inductance of Two Air Core Square Coils with Lateral and Angular Misalignments in a Flat Planar Surface," *IEEE Trans. on Magnetics*, vol. 50, no. 1, Art no. 7000209, Jan. 2014, .

[9] Y. Wang, Y. Yao, X. Liu, D. Xu, "S/CLC Compensation Topology Analysis and Circular Coil Design for Wireless Power Transfer," *IEEE Trans. on Transportation Electrification*, vol. 3, no. 2, pp. 496 – 507, June 2017.

[10] W. Zhang, C. Mi, "Compensation Topologies of High-Power Wireless Power Transfer Systems," *IEEE Trans. on Vehicular Technology*, vol. 65, no. 6, pp. 4768 – 4778, June 2016.

[11] W. Zhang, S. Wong, C. K. Tse, Q. Chen, "Analysis and Comparison of Secondary Series- and Parallel-Compensated Inductive Power Transfer Systems Operating for Optimal Efficiency and Load-Independent Voltage-Transfer Ratio," *IEEE Trans. on Power Electronics*, vol. 29, no. 6, pp. 2979 – 2990, June 2014.

[12] C. Li, Y. Wang, Y. Yao, C. Cecati, X. Zhang, X. Liu, D. Xu, "A novel compensation topology for Inductively Coupled Power Transfer," *Proc. 42nd Annual Conference of the IEEE Industrial Electronics Society (IECON 2016)*, pp. 4471 – 4475, Florence, 2016.

[13] A. Ramezani, S. Farhangi, H. Iman-Eini, B. Farhangi, R. Rahimi, G. R. Moradi, "Optimized LCC-Series Compensated Resonant Network for Stationary Wireless EV Chargers," *IEEE Trans. on Industrial Electronics*, vol. 66, no. 4, pp. 2756–2765, April 2019.

[14] Z. Huang, S. Wong, C. K. Tse, "Design methodology of a series-series inductive power transfer system for electric vehicle battery charger application," *Proc. IEEE Energy Conversion Congress and Exposition (ECCE)*, pp. 1778 – 1782, Pittsburgh, PA, 2014.

[15] Y. Li, M. Yang, Z. He, "Two-Degree-of-Freedom H ∞ Robust Control Optimization for the IPT System With Parameter Perturbations," *IEEE Trans. on Power Electronics*, vol. 33, no. 12, pp. 10954 – 10969, 2018.

[16] S. Samanta, A. K. Rathore, "Small-Signal Modeling and Closed-Loop Control of a Parallel–Series/Series Resonant Converter for Wireless Inductive Power Transfer," *IEEE Trans. on Industrial Electronics*, vol. 66, no. 1, pp. 172-182, Jan. 2019.

[17] S. Zou, O. C. Onar, V. Galigekere, J. Pries, G. Su and A. Khaligh, "Secondary Active Rectifier Control Scheme for a Wireless Power Transfer System with Double-Sided LCC Compensation Topology," *Proc. 44th Annual Conference of the IEEE Industrial Electronics Society (IECON 2018)*, pp. 2145 – 2150, Washington, DC, 2018.

[18] H. Hao, G. A. Covic and J. T. Boys, "An Approximate Dynamic Model of LCL- T-Based Inductive Power Transfer Power Supplies," *IEEE Trans. on Power Electronics*, vol. 29, no. 10, pp. 5554 – 5567, Oct. 2014.

[19] A. K. Swain, M. J. Neath, U. K. Madawala, D. J. Thrimawithana, "A Dynamic Multivariable State-Space Model for Bidirectional Inductive Power Transfer Systems," *IEEE Trans. on Power Electronics*, vol. 27, no. 11, pp. 4772 – 4780, Nov. 2012.

[20] J. Zhao, T. Cai, S. Duan, H. Feng, C. Chen, X. Zhang, "A General Design Method of Primary Compensation Network for Dynamic WPT System Maintaining Stable Transmission Power," *IEEE Trans. on Power Electronics*, vol. 31, no. 12, pp. 8343 – 8358, Dec. 2016.

[21] Z. Huang, S. Wong, C. K. Tse, "Control Design for Optimizing Efficiency in Inductive Power Transfer Systems," *IEEE Trans. on Power Electronics*, vol. 33, no. 5, pp. 4523 – 4534, May 2018.

[22] K. Song, Z. Li, J. Jiang, C. Zhu, "Constant Current/Voltage Charging Operation for Series–Series and Series–Parallel Compensated Wireless Power Transfer Systems Employing Primary-Side Controller," *IEEE Trans. on Power Electronics*, vol. 33, no. 9, pp. 8065 – 8080, Sept. 2018.

[23] A. Berger, M. Agostinelli, S. Vesti, J. A. Oliver, J. A. Cobos, M. Huemer, "A Wireless Charging System Applying Phase-Shift and Amplitude Control to Maximize Efficiency and Extractable Power," *IEEE Trans. on Power Electronics*, vol. 30, no. 11, pp. 6338 – 6348, Nov. 2015.

[24] T. Yeo, D. Kwon, S. Khang and J. Yu, "Design of Maximum Efficiency Tracking Control Scheme for Closed-Loop Wireless Power Charging System Employing Series Resonant Tank," *IEEE Trans. on Power Electronics*, vol. 32, no. 1, pp. 471 – 478, Jan. 2017.

[25] T. Diekhans, R. W. De Doncker, "A Dual-Side Controlled Inductive Power Transfer System Optimized for Large Coupling Factor Variations and Partial Load," *IEEE Trans. on Power Electronics*, vol. 30, no. 11, pp. 6320 – 6328, Nov. 2015.

[26] D. Ahn, S. Kim, J. Moon, I. Cho, "Wireless Power Transfer With Automatic Feedback Control of Load Resistance Transformation," *IEEE Trans. on Power Electronics*, vol. 31, no. 11, pp. 7876 – 7886, Nov. 2016.

[27] J. M. Miller, O. C. Onar, M. Chinthavali, "Primary-Side Power Flow Control of Wireless Power Transfer for Electric Vehicle Charging," *IEEE Journal of Emerging and Selected Topics in Power Electronics*, vol. 3, no. 1, pp. 147 – 162, March 2015.

[28] J. Jiang, K. Song, Z. Li, C. Zhu, Q. Zhang, "System Modeling and Switching Control Strategy of Wireless Power Transfer System," *IEEE Journal of Emerging and Selected Topics in Power Electronics*, vol. 6, no. 3, pp. 1295 – 1305, Sept. 2018.

[29] E. Gati, G. Kampitsis, S. Manias, "Variable Frequency Controller for Inductive Power Transfer in Dynamic Conditions," *IEEE Trans. on Power Electronics*, vol. 32 , no. 2, pp. 1684 – 1696, Feb. 2017.

[30] P. Si, A. P. Hu, S. Malpas, D. Budgett, "A Frequency Control Method for Regulating Wireless Power to Implantable Devices," *IEEE Trans. on Biomedical Circuits and Systems*, vol. 2, no. 1, pp. 22 – 29, Mar. 2008.

[31] M. Yang, Y. Li, H. Du, C. Li, Z. He, "Hierarchical Multiobjective H-Infinity Robust Control Design for Wireless Power Transfer System Using Genetic Algorithm," *IEEE Trans. on Control Systems Technology*, vol. 27, no. 4, pp. 1753 – 1761, Jul. 2019.

[32] C. Xia, W. Wang, G. Chen, X. Wu, S. Zhou, and Y. Sun, "Robust Control for the Relay ICPT System Under External Disturbance and Parametric Uncertainty", *IEEE Trans. on Control Systems Technology*, 25(6), pp. 2168 - 2175, November 2017.

[33] S. R. Sander, J. M. Noworolski, X. Z. Liu, G. C. Verghese, "Generalized averaging method for power conversion circuits," *IEEE Trans. on Power Electronics*, vol. 6, no. 2, pp. 251 – 259, Apr. 1991.

[34] P. Apkarian and D. Noll, "Nonsmooth H-infinity Synthesis," *IEEE Trans. on Automatic Control*, Vol. 51, No. 1, pp. 71 – 86, 2006.

[35] S. Skogestad, "Simple analytic rules for model reduction and PID controller tuning," *Journal of Process Control*, Vol. 13, No. 4, pp. 291 – 309, June 2003.

[36] C. Grimholt, S. Skogestad, "Optimal PI-Control and Verification of the SIMC Tuning Rule," *IFAC Proceedings Volumes*, Vol. 45, No. 3, pp. 11 – 22, 2012.

[37] M. Garcia-Sanz, *Wind Energy Systems: Control Engineering Design*, CRC Press, February 2012.

[38] M. Veerachary, A. R. Saxena, "Design of Robust Digital Stabilizing Controller for Fourth-Order Boost DC–DC Converter: A Quantitative Feedback Theory Approach", *IEEE Trans. on Industrial Electronics*, vol. 59, no. 2, pp. 952 – 963, Feb. 2012.

[39] E. Sadeghi, M. H. Zand, M. Hamzeh, M. Saif, S. M. M. Alavi, "A Controllable Electrochemical Impedance Spectroscopy: From Circuit Design to Control and Data Analysis" *IEEE Trans. on Power Electronics*, 35(9), pp. 9935–9944, 2020.

[40] S. M. M. Alavi, M. J. Hayes, "Quantitative feedback design for a benchmark quadruple-tank process," *IET Irish Signals and Systems Conference*, pp. 401 – 406, 2006.

[41] M. J. Walsh, S. M. M. Alavi, M. J. Hayes, "Practical assessment of hardware limitations on power aware wireless sensor networks—An anti-windup approach,"*Int. J. of Robust and Nonlinear Control*, 20 (2), pp. 194 – 208, 2010.

[42] M. Garcia-Sanz, I. Egana, M. Barreras, "Design of quantitative feedback theory non-diagonal controllers for use in uncertain multiple-input multiple-output systems," *IEE Proceedings of the Control Theory and Applications*, 152(2), pp. 177 – 187, 2005.

[43] B. Labibi, S. M. M. Alavi, "Inversion-free decentralised quantitative feedback design of large-scale systems," *Int. Journal of Systems Science*, 47 (8), pp. 1772 – 1782, 2016.

[44] M. Garcia-Sanz, *Robust control engineering: Practical QFT solutions*, CRC Press, June 2017.

[45] C. Borghesani, Y. Chait, O. Yaniv, "*Quantitative Feedback Theory Toolbox User's Guide,* Terasoft Inc., 1993-2003.

[46] J.T. Boys, G.A. Covic, "The Inductive Power Transfer Story at the University of Auckland," *IEEE Circuit Syst. Mag.*, vol. 15, pp. 6 – 27, 2015.

[47] S. Varikkottil, F. Daya J. L., "Estimation of Optimal Operating Frequency for Wireless EV Charging System under Misalignment," *Electronics*, 8, 342,2019.

[48] M. K. Kazimierczuk, "Class D voltage-switching MOSFET power amplifier," *IEE Proceedings B - Electric Power Applications*, vol. 138, no. 6, pp. 285 – 296, Nov. 1991.

[49] D. Yue, Q.-L. Han, C. Peng, "State Feedback Controller Design of Networked Control Systems," *IEEE Trans. on Circuits and Systems II: Express Briefs*, 51(11), pp. 640 – 644, November 2004.

[50] F. Hao, X. Zhao, "Linear matrix inequality approach to static output-feedback stabilisation of discrete-time networked control systems," *IET Control Theory and Applications*, 4(7), pp. 1211 – 1221, 2010.

[51] S. M. M. Alavi, M. J. Walsh, M. J. Hayes, "Robust power control for IEEE 802.15.4 wireless sensor networks with round-trip time-delay uncertainty,"Wireless Communications and Mobile Computing, 10, pp. 811 -– 825, 2010.

[52] M. Garcia-Sanz, J. G. Guillen, "Smith predictor for uncertain systems in the QFT framework," *In Progress in system and robot analysis and control design*, Springer, London, pp. 239 – 250, 1999.

[53] H. Matsumoto, Y.Neba, H. Asahara, "Switched Compensator for Contactless Power Transfer Systems," *IEEE Transcations on Power Electronics*, 30 (11), pp. 6120 – 6129, 2015.

[54] L. Tan, M. Zhang, S. Wang, S. Pan, Z. Zhang, J. Li, X. Huang, "The Design and Optimization of a Wireless Power Transfer System Allowing Random Access for Multiple Loads," *Energies*, 12, 1017, 2019.

[55] A. C. Zolotas, G.D. Halikias, "Optimal design of PID controllers using the QFT method," *IEE Proceedings Control Theory and Applications*, 146(6), pp. 585-589, 1999.

[56] P. Mercader, K. J. Åström, A. Baños, T. Hägglund, "Robust PID design based on QFT and convex–concave optimization," *IEEE Trans. on Control Systems Technology*, 25(2), 441 – 452, 2016.